Planetary and Space Science 58 (2010) 1758–1765

Contents lists available at ScienceDirect

Planetary and Space Science

journal homepage: www.elsevier.com/locate/pss

Brightness of Saturn's rings with decreasing solar elevation

Alberto Flandes [a,*], Linda Spilker [a], Ryuji Morishima [a], Stuart Pilorz [b], Cédric Leyrat [c], Nicolas Altobelli [d], Shawn Brooks [a], Scott G. Edgington [a]

[a] Jet Propulsion Laboratory/California Institute of Technology, Pasadena, USA
[b] SETI Institute, Mountain View, USA
[c] Observatoire de Paris-LESIA, France
[d] European Space and Astronomy Center, European Space Agency (ESAC/ESA), Madrid, Spain

ARTICLE INFO

Article history:
Received 5 January 2010
Received in revised form
31 March 2010
Accepted 6 April 2010
Available online 18 April 2010

Keywords:
Planetary rings
Rings of Saturn
Thermal studies
Saturn

ABSTRACT

Early ground-based and spacecraft observations suggested that the temperature of Saturn's main rings (A, B and C) varied with the solar elevation angle, B'. Data from the composite infrared spectrometer (CIRS) on board Cassini, which has been in orbit around Saturn for more than five years, confirm this variation and have been used to derive the temperature of the main rings from a wide variety of geometries while B' varied from near -24° to 0° (Saturn's equinox).

Still, an unresolved issue in fully explaining this variation relates to how the ring particles are organized and whether even a simple mono-layer or multi-layer approximation describes this best. We present a set of temperature data of the main rings of Saturn that cover the $\sim 23^\circ$—range of B' angles obtained with CIRS at low ($\alpha \sim 30^\circ$) and high ($\alpha \geq 120^\circ$) phase angles. We focus on particular regions of each ring with a radial extent ≤ 5000 km on their lit and unlit sides. In this broad range of B', the data show that the A, B and C rings' temperatures vary as much as 29–38, 22–34 and 18–23 K, respectively. Interestingly the unlit sides of the rings show important temperature variations with the decrease of B' as well. We introduce a simple analytical model based on the well known Froidevaux monolayer approximation and use the ring particles' albedo as the only free parameter in order to fit and analyze this data and estimate the ring particle's albedo. The model considers that every particle of the ring behaves as a black body and warms up due to the direct energy coming from the Sun as well as the solar energy reflected from the atmosphere of Saturn and on its neighboring particles. Two types of shadowing functions are used. One analytical that is used in the latter model in the case of the three rings and another, numerical, that is applied in the case of the C ring alone. The model lit side albedo values at low phase are 0.59, 0.50 and 0.35–0.38 for the A, B and C rings, respectively.

Published by Elsevier Ltd.

1. Introduction

The main rings of Saturn (A, B and C) can be understood as a vertically thin disk composed of colliding particles covered with an almost pure water ice regolith. Their particle sizes range from centimeters to meters following a power-law size distribution ($q=-3$, French and Nicholson, 2000). The densest and widest of the three main rings, the B ring, sits in the middle of this system from 92 000 to 117 580 km from the center of Saturn. The C ring is much more transparent and narrower than the B ring and spans from 74 658 to 92 000 km, which is divided into an innermost homogenous region and an outermost heterogeneous region (the Plateaus). Beyond the B ring, the Cassini division and the A ring extend radially from 117 516 to 122 170 km and 122 170 to 136 775 km, respectively. The A ring seems to be the most dynamic of the main rings as its many density waves and clumpiness created by self gravitational wakes show.

Since the first detection of the thermal emission of the rings of Saturn at 10 μm in 1969 (Allen and Murdock, 1971), numerous infrared observations have been made and, with them, significant steps in the understanding of the properties and dynamics of the rings have been achieved. Some of the early measurements of the lit side of the rings showed that the rings had temperatures on the order of those of the planet itself, ~ 94 K (Ingersoll et al., 1980), but also suggested that the rings' observed temperatures could vary with the solar elevation angle B' (Murphy, 1973; Nolt et al., 1980) (positive on the north side of the rings and negative otherwise). Although these observations covered different values of B' (6.5–26°), since they were ground-based observations, they were restricted to phase angles (α, Sun-rings-observer angle) $\leq 6^\circ$, thus no temperature variations with α could be determined.

* Corresponding author. Tel.: +1 818 392 0837.
E-mail addresses: flandes@geofisica.unam.mx, aflandes@jpl.nasa.gov (A. Flandes).

0032-0633/$ - see front matter Published by Elsevier Ltd.
doi:10.1016/j.pss.2010.04.002

Early ground-based models describing the rings' temperature dependence on B', assumed either that the ring particles are spread in a single plane or "monolayer" (Froidevaux, 1981) or that the rings are a stack of multiple layers of particles or "multilayer" (Kawata, 1983). Unlike the monolayer approximation, the multilayer model deals with the radiative transfer equation and considers the small-sized particle population contributions. To date, the vertical structure of the rings is not well understood, but a growing body of evidence suggests that, at least, the bigger ring particles may form a monolayer, even in large parts of the A and B rings (Salo, 1995; French and Nicholson, 2000). However, the multilayer model remains applicable for the population of smaller particles that may be easily spread along the vertical direction.

Early models (Froidevaux, 1981; Kawata, 1983) cannot entirely explain the more recent and detailed observations obtained with the Cassini composite infrared spectrometer (CIRS) instrument, in particular, because they were defined considering only ground-based observations and therefore they are restricted to near zero phase angle geometries. On the other hand, recent monolayer (Ferrari et al., 2005; Leyrat et al., 2008) and multilayer (Morishima et al., 2009) models, which are applicable to any observational geometry have been able to explain some of the features of the Cassini CIRS data. Dones et al. (1993) suggest that the A and B rings may be physically thin, such that their multilayer model was unable to reproduce the observed ring phase functions at visible wavelengths and particularly the rings' low reflectivity at large phase angles. Nevertheless, the fraction of small particles may be small, but non-negligible according to observations (Marouf et al., 1983) and the importance of this fraction could grow with the elevation of the observer, $|B|$. The opposition surge seen in photometric observations was explained by the inter-particle shadowing effect of packed ring particles in multilayer models (Lumme et al., 1983). However, recent work by Nelson et al. (1998) and Poulet and Cuzzi (2002) suggests that coherent backscatter, in addition to shadow hiding, may be responsible for the opposition surge observed at low phase angles in visible wavelengths, so that a multilayer model may no longer be needed to explain the strong ring opposition surge. Moreover, self-gravity wake models of Cassini stellar occultation data (Colwell et al., 2006; Hedman and Nicholson, 2007) support a monolayer of the largest particles, but fine-scale dynamical structures have been observed recently (Colwell et al., 2006, 2007), suggesting that, at least, the A and B rings are far from being a homogeneous medium. Still, all these models have demonstrated that, regardless of the intrinsic organization of the ring particles, their albedo, as well as their thermal inertia and spin rate are important physical properties that help to control the temperature of the rings.

In Section 2, we present and explain the data for our study, Section 3 describes the implemented models and equations that explain our data and Section 4 provides the discussion and conclusions.

2. Data reduction

The composite infrared spectrometer (CIRS) consists of two Fourier transform spectrometers, which together measure thermal emission from wavelengths of 1400 to 10 cm^{-1} (7 μm to 1 mm) at spectral resolution programmable from 0.5 to 15.5 cm^{-1} (Kunde et al., 1996; Flasar et al., 2004). The far infrared interferometer (Focal Plane 1, FP1) covers from 600 to 10 cm^{-1} (17 μm to 1 mm) and has a 0.25° field of view. The mid-infrared interferometer consists of two 1×10 arrays of 0.2° pixels, (FP3, FP4) that together span 1400–600 cm^{-1} (7–17 μm). Each ring region contains particles at many orientations and temperatures, and their superimposed emission produces a single spectrum. A simple model for the observed intensity, $I(k)$, leads to an expression in terms of a representative temperature, T, and thermal-derived filling factor β, i.e. $I(k) = \beta B(k,T)$. Here, $B(k,T)$ is the Planck function related to the field of view (FOV) with a surface area σ, that is emitting at a temperature, T and k is the wave number. All CIRS spectra analyzed to date resemble Planck functions so closely that the two parameter fit works exceptionally well (Spilker et al., 2005, 2006). The fit temperature is a representative temperature within the footprint; the parameter, β, is a scaling factor ranging from 0 to 1 that represents the net emissivity of the ring structure. It includes the IR emissivity of the individual particles surfaces, the geometrical cross section, and a component that is dependent upon the temperature distribution within the field of view.

The extensive set of thermal measurements of Saturn's main rings by (CIRS) provides a new information on the rings, since the temperatures are retrieved for the lit and unlit side of the rings over a variety of ring geometries (Spilker et al., 2003) that include α , B', spacecraft elevation B (both with respect to the ring plane) and local hour angle ψ (noon in the direction of the Sun). Saturn equinox took place in August 2009 which allows us to include data that cover from near $B' = 23^\circ$ to 0°. With this new set of data we can get a better picture of the thermal behavior of the rings.

It has been observed that, to first order, the largest temperature changes on the lit face of the rings are driven by variations in α, while differences in temperature with changing B and ψ are a secondary effect (Altobelli et al., 2009); however, important variations in temperature are observed at different radial distances from the planet r_S due to optical depth (τ) and albedo variations. These former considerations are taken into account in order to isolate the effects of B' on the main rings.

A first general approach to the temperature evolution in the main rings with changing solar elevation can be observed in Fig. 1. Fig. 1a shows 12 radial scans of the lit side of the main rings—outside the planet's shadow—from -22° to 0° or Saturn's equinox (see Table 1 for the observation geometry details) where we can see how the temperature falls ~40 K on average. Fig. 1b shows 10 complete radial scans of the unlit side of the main rings, which clearly show a decrease in temperature as well. Notice that both sides reach similar temperatures at equinox and that, on average, the lit/unlit temperature gradient at high solar elevations is near 10 K and that this gradient is inversely correlated with the optical depth (see Table 2 for details on their geometry).

For analysis purposes, we chose regions, in every ring, where τ had quite small variations and selected observations obtained at $r_S \leq 20R_S$ to have control of the footprint size (FOV ~5000 km across, see Table 3 for a summary) such that we observe a single ring alone. In the case of the A ring our footprints fall in a fairly uniform region with normal $\tau \approx 0.63$. For the B ring we chose its optically thickest region ($\tau > 4.0$), but for consistency in our calculations with our monolayer approximation, we use $\tau = 2.374$ as in Hämmen-Anttila and Vaaraniemi, 1975 as maximum possible value) and for the C ring, a fairly homogeneous region outside the plateaus with $\tau \approx 0.08$; these regions are highlighted in Fig. 1a and b with thick lines in the X axis. Moreover, in order to compare footprints where the particles were under the same conditions of illumination, we separated the observations of the lit and the unlit side of every ring and restricted the α and ψ values. We only considered $\alpha \sim 30^\circ$ (low α) and $\alpha \geq 120^\circ$ (high α) as well as ψ outside of the shadow of Saturn (mainly $6:00 \leq \psi \leq 18:00$) to avoid the much colder particles in transit in the shadow or particles heating up after the eclipse.

The available selected data from each ring are shown in Fig. 6a–c and comprise $0^\circ \leq B' \leq -23.5^\circ$. Every point represents the average of the temperatures measured during every scan. In

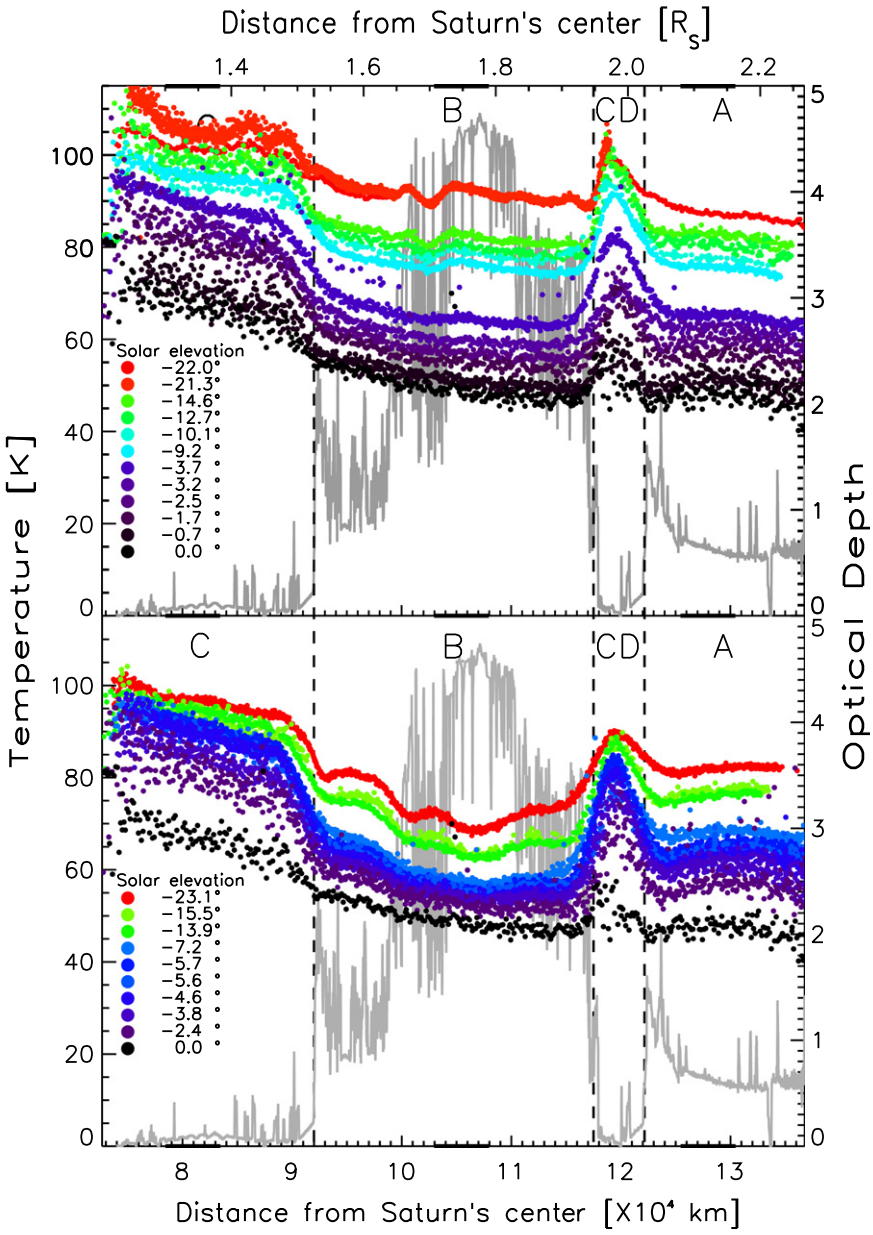

Fig. 1. Cassini CIRS main rings radial scans at different solar elevation angles. (Top) The lit side scans cover an interval of $\sim 22^{\circ}$ from day 104 (14th April) of 2005 to day 224 (12th August) of 2009. (Bottom) The unlit side scans cover a $\sim 23.1^{\circ}$ interval from day 349 (14th December) of 2004 to day 224 (12th August) of 2009. In both cases, the optical depth is added as reference (Colwell et al., 2009). The regions of analysis that we consider in this work for each ring are highlighted on the *X* axis with thicker black lines.

Table 1
Lit side radial scan properties.

Scan	*Year*	*Day*	B' (deg)	α (deg)	B (deg)	ψ (h)
1	2005	104	−22.0	31.1	−7.6	16.0
2	2005	177	−21.3	0.3	−21.6	16.9
3	2006	349	−14.6	25.7	−22.4	7.0
4	2007	115	−12.7	15.2	−24.2	7.0
5	2007	298	−10.1	25.0	−2.6	4.7
6	2007	353	−9.2	35.0	−9.3	14.9
7	2008	347	−3.7	32.9	−9.1	15.4
8	2009	18	−3.2	42.3	−22.1	13.0
9	2009	60	−2.5	56.8	−34.0	13.3
10	2009	115	−1.7	51.4	−23.1	13.4
11	2009	175	−0.7	144.0	−34.4	20.0
12	2009	224	0.0	70.9	20.3	9.5

Table 2
Unlit side radial scan properties.

Scan	*Year*	*Day*	B' (deg)	α (deg)	B (deg)	ψ (h)
1	2004	349	−23.1	52.7	4.1	8.4
2	2006	285	−15.5	66.5	17.2	12.4
3	2007	35	−13.9	47.5	11.7	8.9
4	2008	125	−7.2	22.3	14.9	6.5
5	2008	221	−5.7	28.0	13.0	16.4
6	2008	127	−5.6	41.0	32.5	14.7
7	2008	288	−4.67	31.8	18.5	16.6
8	2008	342	−3.8	29.1	23.0	6.5
9	2009	64	−2.4	45.9	43.4	8.0
10	2009	224	0.0	70.9	20.3	9.5

the case of the B ring unlit side data, all α values were considered, since its temperature variations due to changes in this angle are negligible. IRIS (infrared spectrometer) data from Voyager 2 (triangles) and ground-based data (diamonds) from different authors are added to our sets only for comparison purposes. The Voyager 2 data in the A, B and C rings sets correspond to the August 1981 Saturn flyby, then $B' \sim +8^{\circ}$ and $B \sim +67^{\circ}$. The ground-based data correspond to brightness temperatures of the lit sides of the A and B rings obtained between 1973 and 1982 (Esposito et al., 1984) in the wavelength range of 18−25 μm.

3. Model and equations

In this section, we introduce an analytical model based on the monolayer approximation assuming that the direct solar radiation and the thermal radiation from Saturn are the most relevant heat sources. In contrast to the multilayer approach, in the monolayer model, the determination of the shadowing function, C, which describes how the projected shadow of each ring particle on the others varies is quite important. This variation depends both on B' and τ. Furthermore, a more complete shadowing function should also consider the α and B variations as well. We will use an analytical shadowing function, $C(B',\tau)$, for all three rings and we introduce two numerical shadowing functions, $C(B',\tau,\alpha)$, for the C ring alone.

Table 3
Regions of analysis.

RING	Region of analysis ($\pm$2500 km)	Approximate particle Optical depth (τ)
A	127 954	0.63
B	105 457	2.73
C	80 943	0.08

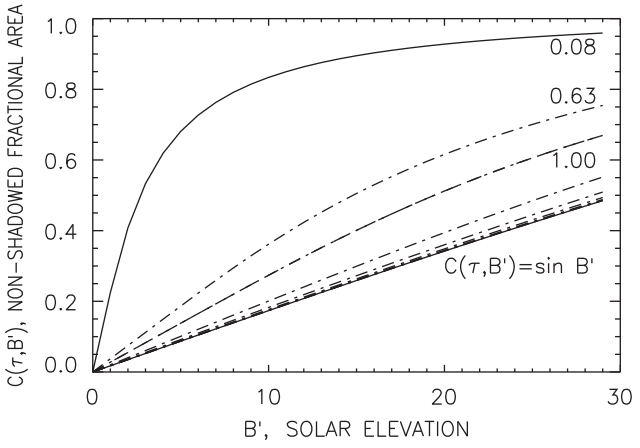

Fig. 2. Shadowing curves for different optical depths. Eq. (1) was used in all cases. The topmost curve corresponds to the C ring. As optical depth increases, the curves approach the function sinB' which coincides with the lambertian approximation.

3.1. Analytical shadowing function

Froidevaux (1981) introduces the function $C(B',\tau)$ or random shadowing function that reproduces the variation of the non-shadowed fractional area of the ring particles with B'. A good approximation of $C(B',\tau)$ is given by Altobelli et al. (2008)

$$C(B',\tau) = \frac{\sin B'}{1-\exp(-\tau)}\left[1-\exp\left(\frac{-\tau}{\sin B'}\right)\right] \quad (1)$$

Note that $\lim_{\tau\to\infty} C(B',\tau) = \sin B'$, i.e. when τ is very large (≥ 1)—or infinite for practical purposes—Eq. (1) reduces to the idealistic lambertian slab model as can be seen in Fig. 2.

3.2. Numerical shadowing function (ray tracing)

For the optically thin C ring alone we propose a numerical $C = C(B',\tau,\alpha)$ function, which we obtain through ray tracing at low and high α values. We chose the C ring because it is optically thin enough to consist of well-separated ring particles which are more straightforward to model while the A and B rings are clumpy and more difficult to model. Ray tracing is a widely used computer graphics technique where images are generated by tracing the path of light rays through pixels in an image plane. Ray tracing can accurately simulate reflection, scattering, refraction and a good number of optical effects with a high degree of realism, which help us to track the shadow behavior on our simulated particles. The ray tracing rendering process was done using the Maya modeling/animation software–by Autodesk—therefore we consider the ray tracing details beyond the scope of this work. We rendered a layer of identical lambertian spherical particles that sit at random positions, whose average distance between neighboring particles, d, can be defined as

$$d = \sqrt{2\pi/\sqrt{3}[1-\exp(-\tau)]} \quad (2)$$

which is obtained from a similar analysis as that in Hämmen-Anttila and Vaaraniemi (1975). This implies that when $\tau = 0.08$, as in the case of the C ring, $d = 6.87$ particle radii. A point light source is set to move in a circular arc, perpendicular to the layer of particles with center at the center of the distribution of particles.

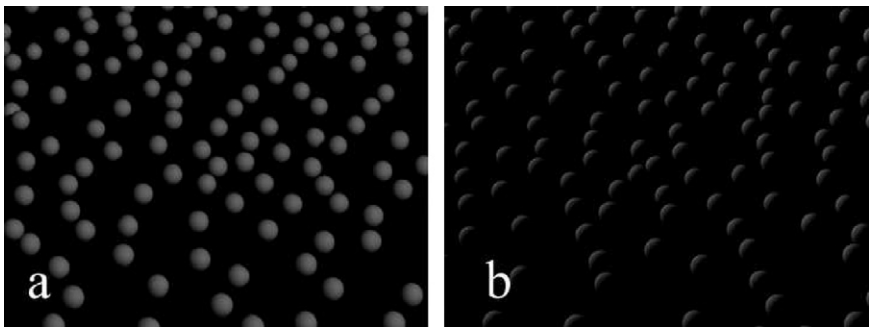

Fig. 3. Ray tracing simulation diagram. The plane of particles is a representation of our FOV in the case of the C ring. In order to represent the different solar elevations (B') our "Sun" moves along the arc of circle from the plane up to 25°. The position of Observer 1 represents the low phase angle $\alpha_{LOW} = 30^{\circ}$ and that of Observer 2 the high phase angle $\alpha_{HIGH} = 120^{\circ}$. Both, Observers 1 and 2 are at fixed B.

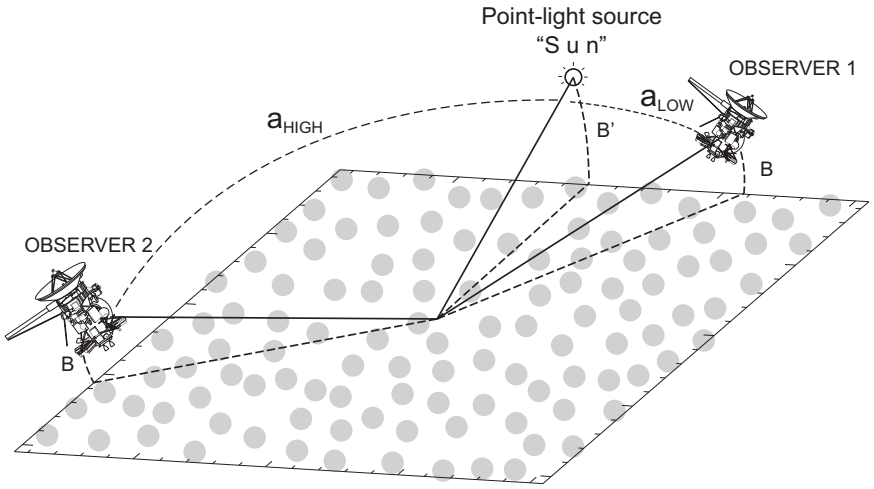

Fig. 4. C ring particle distribution: examples at two different phase angles. The images show two views of the same particle random distribution. The optical depth of the distribution corresponds to 0.08. *a* corresponds to $\alpha = 30^{\circ}$ and *b* to $\alpha = 120^{\circ}$. The Sun is simulated with a point light source at 25° with respect to the layer of particles. Notice that due to the low optical depth, at this high "solar elevation angle" no mutual shadowing is observed.

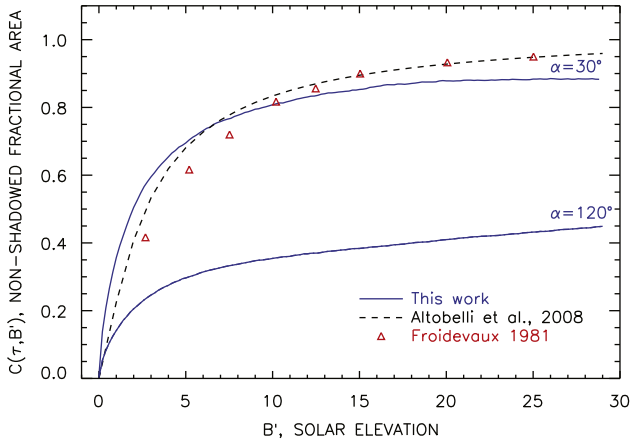

Fig. 5. C ring shadowing functions. Dashed line represents the analytical shadowing function from Eq. (1), triangles are the random shadowing function by Froidevaux (1981). Both latter curves assume a small or near zero degree phase angle. Blue continuous lines correspond to our numerical shadowing functions at low (top) and high (bottom) α values.

The point source moves 25° relative to the ring plane simulating the different positions of the Sun with respect to the ring plane in our range of B' values. We define two points of observation for rendering purposes, one at $\alpha = 30^{\circ}$ and another at $\alpha = 120^{\circ}$. Our FOV is set at the center of the distribution and a snapshot of it is taken every 0.2° (see Fig. 3 for a simplified diagram of our array and Fig. 4 for examples of our FOV at both phase angles when $B' = 25^{\circ}$) as the point light source rises above the layer of particles. From each rendered image, the non-shadowed fraction of the particles is calculated based on a pixel analysis, i.e. each black pixel is assumed to belong to the shadowed fractional area of the particles and any other to belong to the lit fraction or non-shadowed fraction. A comparison between the C ring analytical and numerical shadowing functions (including that from Froidevaux, 1981) is shown in Fig. 5.

3.3. Energy balance equation

In our model, our most relevant heat sources are the direct solar radiation and the thermal radiation from Saturn (F_{sol} and F_{th}, respectively), but the reflected solar energy on Saturn's atmosphere (F_{ref_S}) as well as that reflected and emitted by the ring particles (F_{ref_p} and F_{th_p}) are also taken into account. Explicitly, the equations are as follows:

$$F_{sol} = (1-A_V)C\frac{S_{\odot}}{r^2} \tag{3}$$

$$F_{th} = \sigma T_S^4 \frac{\Omega}{\pi} \tag{4}$$

$$F_{ref_S} = A_S(1-A_V)\frac{S_{\odot}}{r^2}\frac{\Omega}{2\pi}L \tag{5}$$

$$F_{ref_p} = A_V(1-A_V)C\frac{S_{\odot}}{r^2}\frac{\Omega_p}{4\pi} \tag{6}$$

where the energy balance is

$$\sum_i F_i = f\varepsilon\sigma T_p^4\left(1-\frac{\Omega_p}{4\pi}\right) \tag{7}$$

Notice that the mutual thermal flux between the ring particles is included on the left side of Eq. (7). $S_{\odot}$ is the flux received from the Sun at the orbit of Earth (1370 W m^2). A_V and A_S are the bond albedos of the ring particles and Saturn, respectively. A_S is assumed to 0.34 (Atreya, 1986). T_S is Saturn's temperature and T_p is the physical temperature of the particles. r is the footprint's heliocentric distance that varies along the elliptic orbit of Saturn. σ is the Stefan–Boltzmann constant and ε is the particle's thermal emissivity that we assume to be equal to one. We consider the following solid angles: For F_{th}, Ω is the effective angle subtended by the apparent disc of Saturn as seen by the ring particles and calculated through $\Omega = \int\int_S(\vec{r}\cdot\hat{n}\,dS/r^3)$. Ω_p represents the angle subtended by the neighboring particles. For the eight closest neighbors $\Omega_p = 6[1-\exp(-\tau)]$ (Ferrari et al., 2005). Further, f is the rotation rate factor of the particles. Fast rotators can be considered isothermal and thus radiating over their whole surface in which case $f=4$. We only consider slow rotators in our analysis, which are assumed to radiate, on average, over a single hemisphere ($f=2$). Although local time may have a minor effect, in Eq. (5) we add the term L (explicitly $L = 0.5[1+\cos(\psi+\pi)]$) assuming that not all the footprints considered in our analysis sit at noon ($\psi = 180^{\circ}$) or near noon positions and that the reflected energy that the particles receive from the atmosphere of Saturn varies depending on ψ.

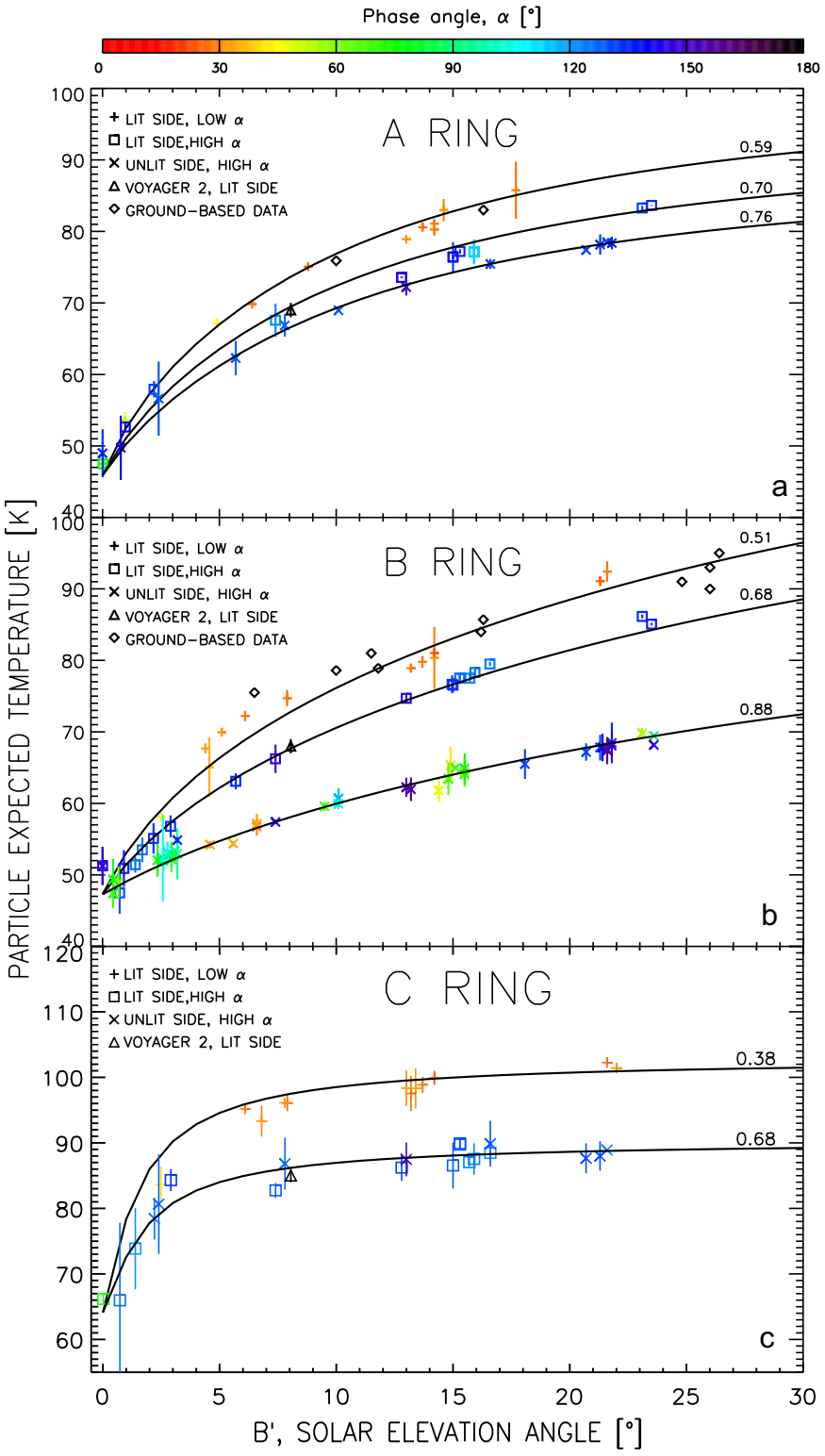

Fig. 6. Cassini CIRS (+, × and □), ground-based (◇) and Voyager 2 (△) data that show the temperature variation with the decrease of the solar elevation angle, B', in the A ring (a), B ring (b) and C ring (c) of Saturn. Data are presented at low ($\alpha \sim 30^{\circ}$) and high ($\alpha \geq 120^{\circ}$) phase angles for the lit and unlit sides. Colors indicate the range of α values according to the top color bar and the error bars represent the observed standard deviation. The analytical model given by Eqs. (1) and (8) was used to fit and explain the CIRS data (only slow rotators, $f=2$, are considered) using the visible bond albedo as the only model parameter. The obtained values are shown on the top right of each curve (see Table 3 as well). The ground-based and Voyager 2 data are only added as reference and were not considered in the fits. In (a) and (b) the three curves represent (from top to bottom) the nonlinear fits for the lit side at low α, the lit side at high α and the unlit side at high α, respectively. In (c) only two fitting curves are shown, one for the lit side at low α (top) and one for the lit/unlit sides simultaneously at high α (bottom) considering a very small or no temperature contrast between both sides of the C ring. Notice also that in the case of the unlit side of the B ring (b, bottom curve) no restriction in phase angle is made.

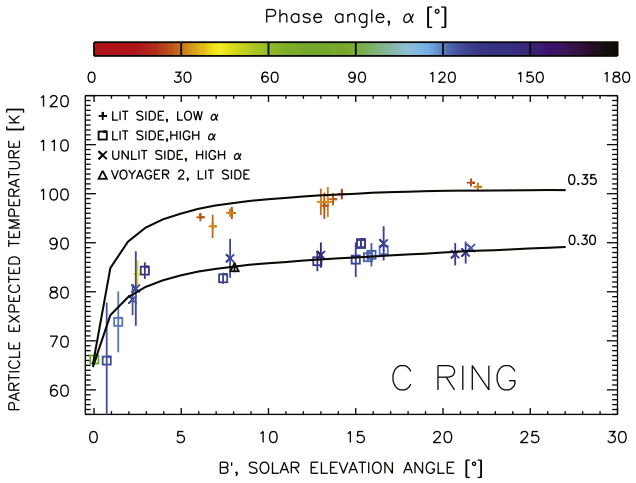

Fig. 7. Cassini CIRS C ring data fits. The C ring data are the same as in Fig. 5 as well as the nomenclature and details. Data were fit with Eq. (8), but in this case, numerical shadowing functions are used in order to account for the phase angle variation. Unlike the C ring fit from the previous figure, the albedo values at low and high phase angles are similar.

Table 4
Model albedo values.

SIDE/α	A	B	C(I)	C(II)
Lit/low	0.59 ± 0.03	0.51 ± 0.07	0.38 ± 0.02	0.35 ± 0.03
Lit/high	0.70 ± 0.06	0.68 ± 0.04	0.63 ± 0.07	0.30 ± 0.04
Unlit/high	0.76 ± 0.05	0.88 ± 0.04	–	–

Let us rewrite Eq. (7) as $T_p^4 = \sum_i F_i/c_0$, where c_0 accounts for all constant terms on the right side. If we write the term $\sum_i F_i$ explicitly using Eqs. (2)–(5) and group all constants (except A_V), as $c_1 = S_\odot c_0^{-1}$, $c_2 = \Omega_p/4\pi$, $c_3 = A_S\Omega/(2\pi)LS_\odot c_0^{-1}$, $c_4 = \sigma T_S^4(\Omega/\pi)c_0^{-1}$, Eq. (6) may be further rewritten as

$$T = \sqrt[4]{(1-A_V)[c_1 C(1+c_2 A_V)+c_3]\frac{1}{r^2}+c_4} \quad (8)$$

We use Eq. (8) to fit our data, assuming A_V as the only free parameter, first using the analytical shadowing function given by Eq. (1) and second, using the numerical functions shown in Fig. 4 (blue continuous curves). We refer to the first case as the "analytical model" and to the second as the "ray tracing model". The analytical model is applied to the lit and unlit side data of the three main rings at low and high α values. The ray tracing model is only applied to the C ring at low and high α values. The resulting curves from both models are shown in Figs. 6 and 7 (analytical model and ray tracing model, respectively). The fitted albedo values from both models also appear in Figs. 6 and 7 to the right of their corresponding curves, but they can be seen in Table 4 as well with their associated errors. These obtained albedo values are also presented and discussed in our conclusions section.

4. Conclusions

4.1. Data highlights

Apart from the difference in the rings' temperature due to phase angle effects, the data show that the temperature of the main rings decreases as B' declines. On average, in the 24° range of values of B', the lit side of the B ring has the largest decrease (near 45.0 K), from 92.4 K at $B' \sim 22°$ to 47.5 K at equinox. The temperatures of the lit side of the A ring, cooler than the B ring lit side temperature at all times, decline almost 40.0 K (from 85.8 to 45.8 K). The C ring temperatures, always warmer than the A and B ring's, decrease almost 36.0 K. The ground-based and Voyager 2 data—introduced only as reference—are consistent with the CIRS data and follow similar variations (Fig. 6). One relevant feature is the difference in temperature between the lit and unlit ring sides which may give us an idea of the main rings' vertical structure. A quite relevant feature is the fact that the temperature of the unlit sides of the rings decreases with B' as well, suggesting that the solar energy that warms the lit sides is transported to the unlit side. The C ring shows no apparent temperature difference between its lit and unlit sides, but the A and B rings show important gradients that decrease with B'. The greatest difference occurs in the optically thick B ring (>16.0 K at high α), while in the A ring is only 7.0 K. The large B ring lit/unlit side gradient supports the idea that its large number of particles are very close together if a monolayer, but if a multilayer, that it may be composed of layers of moderately close particles. The small or near-zero lit/unlit side temperature gradient in the C ring may reinforce the idea that its particles are well separated, such that they are almost equally illuminated at all times. On the other hand, the small vertical gradient of the A ring indicates a much less homogeneous structure if compared to the B and C rings. The energy transport from the lit to the unlit side is inversely correlated to τ and thus, seems to be more efficient in the A ring than in the B ring considering that, in the same range of B' angles, the unlit side temperature of the B ring decreased almost 25% less than that in the case of the A ring (the variations are 22.4 and 29.5 K, respectively). From these sets of data, the equinox—or near equinox—average temperatures are 48, 50 and 65 K for the A, B and C rings, respectively.

4.2. Analytical model

The analytical model applied to the CIRS data reasonably reproduces the observed temperature variations in all three rings at different values of B' and low α (Fig. 5). Though somewhat limited, if compared to other numerical approximations (Morishima et al., 2009), this model may be a useful reference for a practical analysis.

Although the ring particles are mostly composed of water ice, the proportion and type of impurities that they contain are unknown, making the actual albedo values uncertain. The obtained lit side albedo values at low α are 0.59, 0.51 and 0.38 for the A, B and C rings, respectively. Not surprisingly, at high α, we find greater values reflecting an obvious underestimation of the non-shadowed fraction of the ring particles' surfaces, mainly due to the phase angle variation. In this latter case, the albedo values for the lit and unlit sides are—respectively—0.70 and 0.76 for the A ring, 0.68 and 0.88 for the B ring and 0.63 for the C ring, since we use a single fit for both sides considering a very small or no lit/unlit side temperature gradient. For ground-based data ($\alpha < 6°$), Froidevaux (1981) finds 0.60, 0.55 and <0.35 for the A, B and C rings, respectively, assuming slow rotators as well. The same author also reports unrealistically low albedo values (<0.05)—for water ice—if particles are assumed to be fast rotators, which is our case ($A_V \leq 0.12$). The main rings may be likely composed of a mixture of fast and slow rotators with one of these populations dominating in each case. For comparison, multilayer model derived albedo values with a bimodal rotators distribution are 0.51–0.74, 0.55–0.74 and 0.00–0.52 for the A, B and C rings, respectively, from Morishima et al. (2009). Other reference albedo values are 0.52, 0.75 and 0.30 (at around

570 nm) from Porco et al. (2005). From this model, the extrapolated equinox temperatures are 45.92, 47.3 and 64.0 K for the A, B and C rings, respectively. We wish to highlight that the unlit side temperature variation observed in the data justifies the application of the model, but its explanation poses a more complex approach, particularly in the A and B rings, since the transport of energy from the lit to the unlit side may involve particle random spin axes as well as vertical motions. Also in these two rings the wake structure may produce important effects that need to be taken into account.

4.3. Ray tracing model

In regards to the C ring, in Fig. 5 we observe that the low phase angle numerical (top blue curve) and analytical shadowing functions are similar, however, we must bear in mind that the numerical function was calculated at $\alpha = 30^{\circ}$ while the other two functions assume zero or near zero phase angles. In the case of the C ring, better results are obtained through the ray tracing model (Fig. 6) partly because the ray tracing method successfully accounts for the phase angle variation, which is confirmed by the similarity between the different phase angle albedo values. The albedo values at low and high phase angles are 0.35 and 0.30, also consistent with values derived by other authors. A plausible explanation on the discrepancy in these values may be in the fact that only one type of rotators was considered in contrast, the C ring may be likely composed of nearly equal percentage of fast and small rotators (Leyrat et al., 2008).

The present work is a first step towards a more complex model that describes the temperature behavior of the rings at different solar elevations in less restricted and idealized cases, for example a change in the quality of the surfaces of the model particles from smooth to rough or a change in their shapes from spherical to non-spherical or simply irregular would sensibly modify the shadowing conditions and therefore the obtained temperatures. We also left for a future work corrections in the optically thicker and more complex A and B rings that take into account the phase angle variation as we did for the C ring and the temperature contrast between the lit and unlit sides.

Acknowledgements

This research was carried out at the Jet Propulsion Laboratory, California Institute of Technology, under Contract with NASA.

References

Allen, D.A., Murdock, T.L., 1971. Infrared photometry of saturn. Icarus 14, 1.
Altobelli, N., Spilker, L., Leyrat, C., Pilorz, S., 2008. Thermal observations of Saturn's main rings by Cassini CIRS: phase, emission and solar elevation dependence. Planetary and Space Science 56 (1), 134–146.
Altobelli, N., Spilker, L., Leyrat, C., Pilorz, S., Eddgington, S., Wallis, B., Flandes, A., 2009. Thermal phase curves observed in Saturn's main rings by Cassini-CIRS: detection of an opposition effect? Geophysical Research Letters 36 (10) CiteID L10105.
Atreya, S.K., 1986. Atmospheres and ionospheres of the outer planets and their satellites. In: Physics and Chemistry in Space, second ed., vol. 15. Springer-Verlag, Münster, Germany.
Colwell, J.E., Nicholson, P.D., Tiscareno, M.S., Murray, C., French, R.G., Marouf, E.A., 2009. The Structure of Saturn's Rings IN Saturn from Cassini- Huygens, 1st ed., Springer, Dordrecht, Heidelberg, London, New York.
Colwell, J.E., Esposito, L.W., Sremčevič, M., Stewart, G.R., McClintock, W.E., 2006. Self-gravity wakes in Saturn's a ring measured by stellar occultations from Cassini. Geophysical Research Letters 33 (7) CiteID L07201.
Colwell, J.E., Esposito, L.W., Sremčevič, M., Stewart, G.R., McClintock, W.E., 2007. Self-gravity wakes and radial structure of Saturn's B ring. Icarus 190 (1), 127–144.
Dones, L., Cuzzi, J.N., Showalter, M.R., 1993. Voyager photometry of Saturn's a ring. Icarus 105 (1), 184–215.
Esposito, L.W., Cuzzi, J.N., Holberg, J.B., Marouf, E.A., Tyler, G.L., Porco, C.C., 1984. Saturn's rings—structure, dynamics, and particle properties. In: Saturn (A85-33976 15-91). University of Arizona Press, Tucson, AZ.
Ferrari, C., Galdemard, P., Lagage, P.O., Patin, E., Quoirin, C., 2005. Imaging Saturn's rings with camiras, thermal inertia of b and c rings. Astronomy and Astrophysics 441 (1), 379–389.
Flasar, M., Kunde, V.G., Abbas, M.M., Achterberg, R.K., Ade, P., Barucci, A., Bézard, B., Bjoraker, G.L., Brasunas, J.C., Calcutt, S., Carlson, R., Césarsky, C.J., Conrath, B.J., Coradin, A., Courtin, R., Coustenis, A., Edberg, S., Edgington, S., Ferrari, C., Fouchet, T., Gautier, D., Gierasch, P.J., Grossman, K., Irwin, P., Jennings, D.E., Lellouch, E., Mamoutkine, A.A., Marten, A., Meyer, J.P., Nixon, C.A., Orton, G.S., Owe, T.C., Pearl, J.C., Prangé, R., Raulin, F., Read, P.L., Romani, P.N., Samuelson, R.E., Segura, M.E., Showalter, M.R., Simon-Miller, A.A., Smith, M.D., Spencer, J.R., Spilker, L.J., Taylor, F.W., 2004. Exploring the Saturn system in the thermal infrared: the composite infrared spectrometer. Space Science Reviews 115, 169–297.
French, R.G., Nicholson, P.D., 2000. Saturn's rings II. Particle sizes inferred from stellar occultation data. Icarus 145, 502–523.
Froidevaux, L., 1981. Saturn's rings: infrared brightness variation with solar elevation. Icarus 46, 4–17.
Hämmen-Anttila, K.A., Vaaraniemi, P., 1975. A theoretical photometric function of Saturn's rings. Icarus 25, 470–478.
Hedman, M.M., Nicholson, P.D., Salo, H., Wallis, B.D., Burratti, B.J., Baines, K.H., Brown, R.H., Clark, R.N., 2007. Self-gravity wake structures in Saturn's a ring revealed by Cassini- VIMS. The Astronomical Journal 133 (6), 2624–2629.
Ingersoll, A.P., Orton, G.S., Munch, G., Chase, N.S.C., 1980. Pioneer Saturn infrared radiometer—preliminary results. Science 207, 439–443.
Kawata, Y., 1983. Infrared brightness temperature of Saturn's rings based on the inhomogeneous multilayer assumption. Icarus 133, 453–464.
Kunde, V., Ade, P.A., Barney, R.D., Bergman, D., Bonnal, J.F., Borelli, R., Boyd, D., Brasunas, J.C., Brown, G., Calcutt, S.B., Carroll, F., Courtin, R., Cretolle, J., Crooke, J.A., Davis, M.A., Edberg, S., Fettig, R., Flasar, M., Glenar, D.A., Graham, S., Hagopian, J.G., Hakun, C.F., Hayes, P.A., Herath, L., Spilker, L., Jennings, D.E., Karpati, G., Kellebenz, C., Lakew, B., Lindsay, J., Lohr, J., Lyons, J.J., Martineau, R.J., Martino, A.J., Matsumura, M., McCloskey, J., Melak, T., Michel, G., Morell, A., Mosier, C., Pack, L., Plants, M., Robinson, D., Rodriguez, L., Romani, P., Schaefer, W.J., Schmidt, S., Trujillo, C., Vellacott, T., Wagner, K., Yun, D., 1996. Cassini infrared Fourier spectroscopic investigation. In: Cassini/Huygens: A Mission to the Saturnian Systems, Horn L (ed.), Proceedings of SPIE, vol. 2803, pp. 162–177.
Leyrat, C., Ferrari, C., Charnoz, S., Decriem, J., Spilker, L.J., Pilorz, S., 2008. Spinning particles in Saturn's c ring from mid-infrared observations: pre-Cassini mission results. Icarus 196 (2), 625–641.
Lumme, K., Irvine, W.M., Esposito, L.W., 1983. Theoretical interpretation of the ground-based photometry of Saturn's b ring. Icarus 53, 174–184.
Marouf, E.A., Tyler, G.L., Zebker, H.A., Simpson, R.A., Eshleman, V.R., 1983. Particle size distributions in Saturn's rings from voyager 1 radio occultation. Icarus 54, 189–211.
Morishima, R., Salo, H., Ohtsuki, K., 2009. A multilayer model for thermal infrared emission of Saturn's rings: basic formulation and implications for earth-based observations. Icarus 201 (2), 634–654.
Murphy, R.E., 1973. Temperatures of Saturn's rings. The Astronomical Journal 181, L87–L90.
Nelson, R.M., Hapke, B.W., Smythe, W.D., Horn, L.J., 1998. Phase curves of selected particulate materials: the contribution of coherent backscattering to the opposition surge. Icarus 131, 223–230.
Nolt, I.G., Barrett, E.W., Caldwell, J., F.C., Gillett, Murphy, R.E., Radostitz, J.V., Tokunaga, A.T., 1980. IR brightness and eclipse cooling of Saturn's rings. Nature 283, 842–843.
Porco, C.C., Baker, E., Barbara, J., Beurle, K., Brahic, A., Burns, J.A., Charnoz, S., Cooper, N., Dawson, D.D., Genio, A.D.D., Denk, T., Dones, L., Dyudina, U., Evans, M.W., Giese, B., Grazier, K., Helfenstein, P., Ingersoll, A.P., Jacobson, R.A., Johnson, T.V., McEwen, A., Murray, D., Neukum, G., Owen, W.M., Perry, J., Roatsch, T., Spitale, J., Squyres, S., Thomas, P., Tiscareno, M., Turtle, E., Vasavada, A.R., Veverka, J., Wagner, R., West, R., 2005. Cassini imaging science: initial results on Saturn's rings and small satellites. Science 307 (5713), 1237–1242.
Poulet, F., Cuzzi, J.N., 2002. The composition of Saturn's rings. Icarus 160 (2), 350–358.
Salo, H., 1995. Simulations of dense planetary rings. III. Self-gravitating identical particles. Icarus 117, 287–312.
Spilker, L.J., Ferrari, C., Cuzzi, J.N., Showalter, M., Pearl, J., Wallis, B., 2003. Saturn's rings in the thermal infrared. Planetary and Space Science 51, 929–935.
Spilker, L.J., Pilorz, S., Wallis, B., Eddgington, S., Pearl, J., Flasar, F.M., 2005. Saturn ring temperature roll-off at submillimeter wavelengths from Cassini CIRS observations. Earth Moon Planets 96 (3–4), 149–163.
Spilker, L.J., Pilorz, S., Wallis, B., Pearl, J., Cuzzi, J.N., Brooks, S., Altobelli, N., Eddgington, S., Showalter, M., Flasar, F.M., Ferrari, C., Leyrat, C., 2006. Cassini thermal observations of Saturn's main rings: implications for particle rotation and vertical mixing. Planetary and Space Science 54, 1167–1176.